Velocity distributions and aging in a cooling granular gas

Syed Rashid Ahmad and Sanjay Puri
School of Physical Sciences, Jawaharlal Nehru University, New Delhi 110067, India
(Received 3 August 2006; published 6 March 2007)

We use large-scale molecular dynamics simulations to study freely evolving granular gases with dimensionality $d=2,3$. The system dissipates kinetic energy (or *cools*) due to inelastic collisions between granular particles. The density and velocity fields are approximately homogeneous at early times, and the system is said to be in a *homogeneous cooling state* (HCS). However, fluctuations in the density and velocity fields grow, and the system evolves into an *inhomogeneous cooling state* (ICS). We study the nature of velocity distributions in both the HCS and ICS. We also investigate the *aging* property of the velocity autocorrelation function.

DOI: 10.1103/PhysRevE.75.031302 PACS number(s): 45.70.Mg

I. INTRODUCTION

There has been intense research interest in the static and dynamical properties of *granular materials* or *powders* [1–7]. These materials exhibit properties which are intermediate to those of fluids and solids. The understanding and characterization of these properties poses both scientific and technological challenges. One of the most important features of granular materials is that the grains undergo inelastic collisions, with the normal component of velocity being dissipated on collision. This suggests two classes of dynamical problems in the context of powders.

(a) The first class of problems concerns systems where the energy dissipation is compensated by energy input from external driving. Thus the system settles into a nonequilibrium steady-state behavior, which is usually characterized by complex pattern dynamics. There are various standard geometries for driving granular materials, e.g., horizontal or vertical vibration on a platform [8], pouring through a chute [9], rotation in a drum [10–12], etc. These experimental systems give rise to diverse examples of pattern formation, which have attracted much research attention.

(b) The second class of problems concerns the nonequilibrium relaxation of an energized powder in the absence of an external drive. The best-known problem in this class is the *cooling* of an initially homogeneous system of inelastic particles. The inelastic collisions between particles result in the loss of kinetic energy (or cooling), and the local parallelization of particle velocities. In the early stages, the density field is approximately uniform and the system loses energy in a *homogeneous cooling state* (HCS) [13]. However, the HCS is unstable to fluctuations in the density and velocity fields, and the system evolves into an *inhomogeneous cooling state* (ICS) [14–21]. The ICS is characterized by the emergence and growth of particle-rich clusters, with particles in a cluster moving in approximately parallel directions.

In this paper, we study the HCS and ICS of a granular gas through large-scale molecular dynamics (MD) simulations. In earlier work [20], we have characterized pattern formation in the ICS for a two-dimensional inelastic gas via physical quantities like the *correlation function* and *structure factor* for the density and velocity fields; and the growth laws for fluctuations in these fields. Here, we focus on the velocity distributions in the HCS and ICS for cases with dimensionality $d=2,3$. (In a recent letter [22], we have already presented some results in this context.) For an elastic hard-sphere gas, an arbitrary velocity distribution rapidly evolves to the Maxwell-Boltzmann (MB) distribution. However, the situation is not so simple for granular materials with non-MB distributions, e.g., power laws, stretched exponentials, etc., being reported in various studies [1–7]. In this paper, we also study the autocorrelation function of the velocity field. The nonequilibrium evolution of the granular gas gives rise to *aging* or *nonstationary* behavior of the autocorrelation function, which we discuss here.

This paper is organized as follows. In Sec. II, we review the phenomenology of the cooling problem. In Sec. III, we present detailed numerical results from our MD simulations. As mentioned above, we will focus on the nature of velocity distributions in the HCS and ICS, and the aging of the velocity autocorrelation function. Finally, Sec. IV concludes this paper with a summary and discussion.

II. PHENOMENOLOGY OF THE COOLING PROBLEM

A. Homogeneous cooling state (HCS)

The HCS was first studied by Haff [13] and corresponds to an approximately uniform state of the granular gas. We consider an inelastic gas with identical particles (hard spheres) of mass $m=1$ and diameter $\sigma=1$. Consider a collision between particles labeled i and j. The postcollision velocities of the particles are given in terms of the precollision velocities by the following rule:

$$\vec{v}_i' = \vec{v}_i - \frac{1+e}{2}[\hat{n}\cdot(\vec{v}_i - \vec{v}_j)]\hat{n},$$

$$\vec{v}_j' = \vec{v}_j + \frac{1+e}{2}[\hat{n}\cdot(\vec{v}_i - \vec{v}_j)]\hat{n}, \tag{1}$$

where e (<1) is the coefficient of restitution. Here, $\hat{n}$ is a unit vector parallel to the relative position of the particles, and points from j to i at the time of collision.

The granular temperature is defined as $T=\langle\vec{v}^2\rangle/d$, where $\langle\vec{v}^2\rangle$ is the mean-squared velocity. The homogeneous state cools with time t as

$$\frac{dT}{dt} = -\frac{\epsilon\omega(T)T}{d}, \quad \epsilon = 1 - e^2, \tag{2}$$

where $\omega(T)$ is the collision frequency at temperature T. From kinetic theory, this has the approximate form [23]

$$\omega(T) \simeq \frac{2\pi^{(d-1)/2}}{\Gamma(d/2)}\chi(n)nT^{1/2}, \tag{3}$$

where $\chi(n)$ is the pair correlation function at contact for hard spheres with density n. Equations (2) and (3) yield Haff's cooling law for the HCS:

$$T(t) = T_0\left[1 + \frac{\epsilon\omega(T_0)}{2d}t\right]^{-2}, \tag{4}$$

where T_0 is the initial temperature. A useful quantity is the average number of collisions $\tau(t)$ that a particle suffers until time t. This is computed as

$$\tau(t) = \int_0^t dt'\,\omega(t') = \frac{2d}{\epsilon}\ln\left[1 + \frac{\epsilon\omega(T_0)}{2d}t\right]. \tag{5}$$

The number of collisions increases logarithmically (rather than linearly) with time as the system cools with time. In terms of the collision time τ, Haff's cooling law has a particularly simple form:

$$T(\tau) = T_0\exp\left(-\frac{\epsilon}{d}\tau\right). \tag{6}$$

The natural framework to study velocity distributions in the HCS is the inelastic version of the Boltzmann transport equation [7]. In the elastic case ($e=1$), an arbitrary initial distribution rapidly evolves ($\sim$ few particle collisions) to the MB distribution:

$$P_{\mathrm{MB}}(\vec{v}) = \left(\frac{1}{\pi v_0^2}\right)^{d/2}\exp\left(-\frac{\vec{v}^2}{v_0^2}\right), \quad v_0^2 = \frac{2\langle\vec{v}^2\rangle}{d}. \tag{7}$$

Here, $\vec{v}=(v_x,v_y,\ldots)$ denotes the particle velocity. In the near-elastic case ($e\simeq 1$), it has been argued that the distribution function is time-dependent due to the cooling process, but has a scaling form which deviates from the MB function [24,25]:

$$P(\vec{v},t) = \frac{1}{v_0^d(t)}F\left[\frac{\vec{v}}{v_0(t)}\right] \equiv \frac{1}{v_0^d(t)}F(\vec{c}). \tag{8}$$

Here, $v_0^2(t)=2\langle\vec{v}^2\rangle/d$ as before, and

$$F(\vec{c}) = \frac{1}{\pi^{d/2}}\exp(-c^2)\sum_{n=0}^{\infty} a_n S_n(c^2). \tag{9}$$

In Eq. (9), $F(\vec{c})$ has been expanded in terms of the Sonine polynomials, which satisfy the orthogonality relation:

$$\int_0^\infty dc c^{d-1}\exp(-c^2)S_n(c^2)S_m(c^2) = \delta_{nm}\frac{\Gamma(n+d/2)}{2n!}. \tag{10}$$

The first few Sonine polynomials (which we will use in this paper) are

$$S_0(c^2) = 1, \tag{11}$$

$$S_1(c^2) = \frac{d}{2} - c^2, \tag{12}$$

$$S_2(c^2) = \frac{d(d+2)}{8} - \frac{(d+2)}{2}c^2 + \frac{c^4}{2}, \tag{13}$$

$$S_3(c^2) = \frac{d(d+2)(d+4)}{48} - \frac{(d+2)(d+4)}{8}c^2 + \frac{(d+4)}{4}c^4 - \frac{c^6}{6}, \tag{14}$$

$$S_4(c^2) = \frac{d(d+2)(d+4)(d+6)}{384} - \frac{(d+2)(d+4)(d+6)}{48}c^2 + \frac{(d+4)(d+6)}{16}c^4 - \frac{(d+6)}{12}c^6 + \frac{c^8}{24}, \tag{15}$$

$$S_5(c^2) = \frac{d(d+2)(d+4)(d+6)(d+8)}{3840} - \frac{(d+2)(d+4)(d+6)(d+8)}{384}c^2 + \frac{(d+4)(d+6)(d+8)}{96}c^4 - \frac{(d+6)(d+8)}{48}c^6 + \frac{(d+8)}{48}c^8 - \frac{c^{10}}{120}, \text{ etc.} \tag{16}$$

The coefficients a_n in Eq. (9) quantify the deviation from the MB function. The normalization condition dictates $a_0=1$. Further, a simple scaling argument yields $a_1=0$ [7]. The first nontrivial coefficient in the expansion is a_2, and this has been calculated from kinetic theory by Noije and Ernst (NE) [25] as

$$a_2 = \frac{16(1-e)(1-2e^2)}{9+24d+8de-41e+30(1-e)e^2}. \tag{17}$$

The above scenario is only reasonable in the absence of correlations in the HCS, as the Boltzmann equation is only valid in this limit. Brey *et al.* [26] have performed Monte Carlo (MC) simulations of the inelastic Boltzmann equation, and confirmed the validity of Eq. (17). However, it is more relevant to study the applicability of these results in a cooling granular gas. In this context, Huthmann *et al.* [27] have undertaken MD simulations of inelastic hard spheres in $d=2$. They evolved the system from an MB velocity distribution and studied the evolution of the coefficient $a_2(t)$. In general, the coefficients $a_n(t)$ are obtained from the expansion:

$$\langle c^{2k}\rangle(t) = \langle c^{2k}\rangle_{\mathrm{MB}}\sum_{n=0}^{k}(-1)^n\frac{k!}{n!(k-n)!}a_n(t),$$

$$\langle c^{2k}\rangle_{\mathrm{MB}} = \frac{\Gamma(k+d/2)}{\Gamma(d/2)}. \tag{18}$$

This yields the first few a_n's as follows:

$$a_1(t) = 1 - \frac{\langle c^2 \rangle}{\langle c^2 \rangle_{\rm MB}} = 0, \tag{19}$$

$$a_2(t) = -1 + \frac{\langle c^4 \rangle}{\langle c^4 \rangle_{\rm MB}}, \tag{20}$$

$$a_3(t) = 1 + 3a_2 - \frac{\langle c^6 \rangle}{\langle c^6 \rangle_{\rm MB}}, \tag{21}$$

$$a_4(t) = -1 - 6a_2 + 4a_3 + \frac{\langle c^8 \rangle}{\langle c^8 \rangle_{\rm MB}}, \tag{22}$$

$$a_5(t) = 1 + 10a_2 - 10a_3 + 5a_4 - \frac{\langle c^{10} \rangle}{\langle c^{10} \rangle_{\rm MB}}, \text{ etc.} \tag{23}$$

Huthmann *et al.* found that $a_2(t)$ evolved from $a_2=0$ (the MB value) to a "steady-state" value which was consistent with kinetic theory. However, the kinetic-theory prediction was not valid in the ICS, and a_2 relaxed back to zero on a time scale $\tau \sim 30$ collisions for $e=0.4 \ll 1$ (see Fig. 9 of Ref. [27]). Similar results were obtained by Nakanishi [21], who found that the "steady state" was transient even for values of e very close to 1. This is associated with the buildup of correlations prior to the onset of the clustering state, which we will discuss next. Further, Nakanishi found that the deviation from the kinetic-theory prediction occurred considerably earlier than the formation of visible clusters in the density field.

In recent work, Brilliantov and Poschel (BP) [28,29] have used a more sophisticated expansion than NE [25] to calculate the first two nontrivial Sonine coefficients (a_2 and a_3) in the HCS. The BP calculation accounts for the influence of a_3, which is assumed to be negligible in the NE study. They obtain the following expressions in $d=2$ [29]:

$$a_2 = -\frac{16}{b(e)}(-849 + 1170e - 291e^2 + 708e^3 + 2782e^4 - 6400e^5 + 3120e^6 - 480e^7 + 240e^8), \tag{24}$$

$$a_3 = -\frac{128}{b(e)}(183 - 342e - 543e^2 + 1340e^3 + 66e^4 - 1344e^5 + 720e^6 - 160e^7 + 80e^8), \tag{25}$$

$$b(e) = 102\,195 - 128\,358e + 70\,017e^2 + 9060e^3 + 15\,950e^4 - 74\,240e^5 + 34\,800e^6 - 5600e^7 + 2800e^8. \tag{26}$$

The corresponding $d=3$ results are [28]

$$a_2 = -\frac{16}{c(e)}(-1623 + 1934e + 895e^2 - 364e^3 + 3510e^4 - 7424e^5 + 3312e^6 - 480e^7 + 240e^8), \tag{27}$$

$$a_3 = -\frac{128}{c(e)}(217 - 386e - 669e^2 + 1548e^3 + 154e^4 - 1600e^5 + 816e^6 - 160e^7 + 80e^8), \tag{28}$$

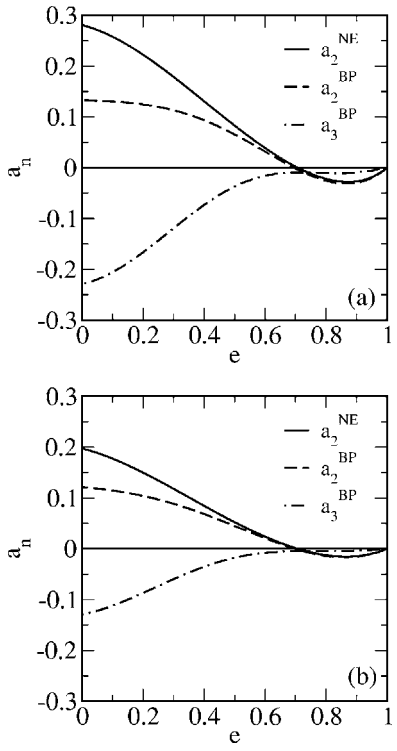

FIG. 1. (a) Plot of analytical expressions for a_2 and a_3 in $d=2$. For a_2, we show the Noije-Ernst (NE) result in Eq. (17) (Ref. [25]); and the Brilliantov-Poschel (BP) result in Eq. (24) (Ref. [29]). For a_3, we show the BP result in Eq. (25) (Ref. [29]). (b) Analogous to (a) but for $d=3$. We plot the NE result for a_2 in Eq. (17); the BP result for a_2 in Eq. (27) (Ref. [28]); and the BP result for a_3 in Eq. (28) (Ref. [28]).

$$c(e) = 214\,357 - 172\,458e + 112\,155e^2 + 25\,716e^3 - 4410e^4 - 84\,480e^5 + 34\,800e^6 - 5600e^7 + 2800e^8. \tag{29}$$

We will subsequently compare our MD data with the results obtained by NE and BP. In Fig. 1(a), we plot a_2 and a_3 versus e for $d=2$ and $e \in [0,1]$. We compute a_2 using the NE result in Eq. (17) (solid line) and the BP result in Eq. (24) (dashed line). Our MD results in this paper are obtained for $e \in [0.7,1]$. For these values of e, there is little difference between $a_2^{\rm NE}$ and $a_2^{\rm BP}$. Further, the typical values of a_3 are 4 to 5 times smaller than the corresponding a_2. Figure 1(b) is the three-dimensional (3D) counterpart of Fig. 1(a).

Before discussing the ICS, we mention that the tail of the distribution function does not obey a MB behavior, but rather decays exponentially as $F(\vec{c}) \sim \exp(-Ac)$, where A is a constant. This is referred to as *overpopulation of the tail* and was first studied by Esipov and Poschel [30] and van Noije and Ernst [25]. It has been confirmed in MC simulations of the Boltzmann equation by Brey *et al.* [26], and also in MD simulations by Huthmann *et al.* [27].

B. Inhomogeneous cooling state (ICS)

As mentioned earlier, the HCS is unstable to fluctuations in both the velocity and density fields. This is depicted in Fig. 2, which shows the evolution of these fields for a two-

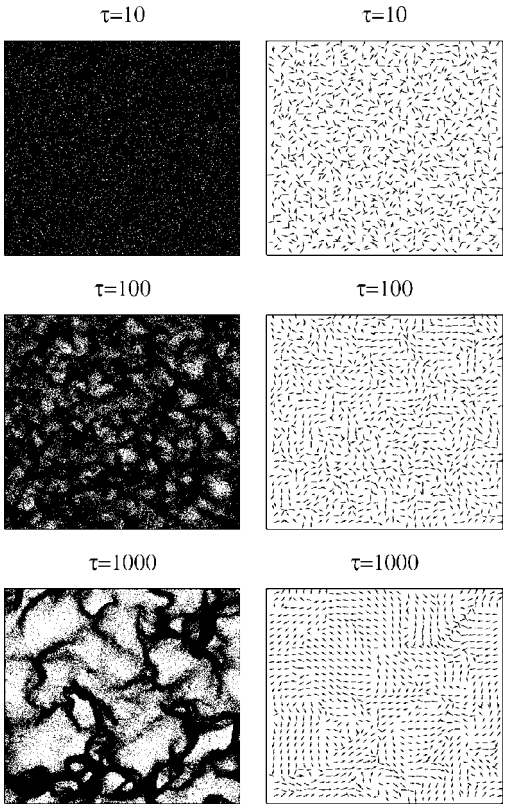

FIG. 2. Evolution snapshots of the density field (frames on left) and velocity field (frames on right) for an inelastic granular gas in $d=2$. These pictures are obtained for a system with particle number $N=262\,144$, packing fraction $\phi\simeq 0.157$, and restitution coefficient $e=0.9$. The size of the system is $(1144.86\sigma)^2$. The details of the MD simulation are provided in the text. The density field is obtained by directly plotting the particle positions. The velocity field is obtained by coarse-graining the system into boxes of size $(17.9\sigma)^2$ and plotting the overall velocity vector for each box.

dimensional (2D) granular gas with $e=0.9$. Correlations develop in the velocity field because particle collisions dissipate the normal component and parallelize the particle velocities. Of course, the overall momentum is conserved, and this must be reflected in the ordered state also. The formation of particle clusters can also be understood on simple physical grounds. Consider a density fluctuation in the HCS. In the denser regions, there is a more rapid collision of particles and faster cooling than in the dilute region. Thus the pressure becomes lower in the denser regions, and particles are sucked into these regions, reinforcing the density fluctuation.

The nature of these instabilities can be clarified by a linear stability analysis of the corresponding nonlinear hydrodynamic equations. A detailed discussion of the instabilities has been given by Brito and Ernst [31] and van Noije and Ernst [32]. Essentially, pattern dynamics in the velocity field is driven by a long-wavelength instability in the *shear mode* for wave vectors $k<k_{\perp}^{c}(\epsilon)\sim\sqrt{1-e^2}$ for $e\to 1$. Similarly, clustering in the density field is driven by long-wavelength (small-k) instabilities in the *heat mode*. The critical wave vector for heat modes is denoted as $k_H^c(\epsilon)$, and satisfies $k_H^c(\epsilon)<k_{\perp}^{c}(\epsilon)$. Again, we have $k_H^c(\epsilon)\sim\sqrt{1-e^2}$ for $e\to 1$. Thus the system size L determines the instabilities which are observed.

(a) For $L<2\pi/k_{\perp}^{c}(\epsilon)$, there is no pattern formation in either the velocity or density fields. In this case, the system always remains in the HCS.

(b) For $2\pi/k_{\perp}^{c}(\epsilon)<L<2\pi/k_H^c(\epsilon)$, the system is characterized by vortex formation in the velocity field but no density inhomogeneities are formed. Again, the system remains in the HCS for all times.

(c) For $2\pi/k_H^c(\epsilon)<L$, the granular gas exhibits both vortex formation and clustering.

The time scale of the shear instability is considerably faster than that of the heat mode. Thus there is a regime of vortex-mediated dynamics in the HCS before the crossover to the ICS. Here, we are interested in the thermodynamic limit with $L\to\infty$, where the asymptotic state of the granular gas is the ICS. In recent work, Das and Puri (DP) [20] have studied pattern dynamics in the nonlinear ICS regime. They have drawn analogies between the clustering process in granular gases and phase-separation kinetics in binary mixtures. DP characterized pattern formation in the velocity and density fields via the domain growth laws, and the scaling behavior of the time-dependent correlation functions and structure factors. DP argued that the *streaming-and-aggregation* dynamics of the granular gas results in conservation on the cluster length scale, which diverges with time. Thus the asymptotic dynamics obeys a global conservation law, which is a much weaker constraint than a local conservation law. In related work, Wakou *et al.* [33] have demonstrated that the evolution of the granular flow field can be described via a time-dependent Ginzburg-Landau equation for a nonconserved order parameter.

In this paper, our primary interest is the nature of the velocity distribution functions in the HCS and ICS, and the aging behavior of the velocity autocorrelation function. In Sec. II A, we have mentioned that there is some understanding of the non-MB velocity distributions in the HCS. However, we do not have a similar understanding of the velocity distributions in the ICS. In the next section, we present detailed numerical results to clarify velocity distributions in the ICS for granular gases in $d=2,3$.

III. NUMERICAL RESULTS FROM MOLECULAR DYNAMICS SIMULATIONS

A. Details of simulations

We used event-driven MD to simulate a system of inelastically colliding particles [34,35]. The particles were identical with mass $m=1$ and diameter $\sigma=1$. We did not consider the rotational motion of the particles. The relation between precollision and postcollision velocities is given in Eq. (1). The granular gas consisted of $N=10^6$ particles confined in a 2D or 3D box with periodic boundary conditions. The box sizes were chosen so that the number fraction was $\rho=0.2$ in both cases, with packing fraction $\phi\simeq 0.157$ in $d=2$ and $\phi\simeq 0.105$ in $d=3$. (In an earlier study, Kawahara and Nakanishi [36] have investigated the free cooling of an inelastic gas

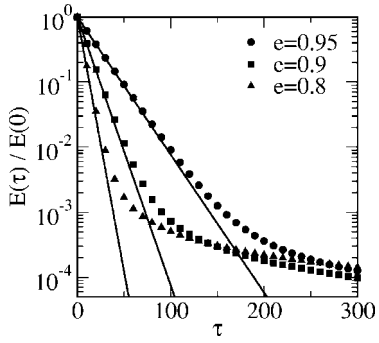

FIG. 3. Time-dependence of the granular temperature in $d=2$, shown on a linear-log scale. We plot the normalized kinetic energy $E(\tau)/E(0)$ vs τ for $e=0.95$, 0.9, and 0.8. The solid lines denote Haff's law from Eq. (6).

with $N=0.5\times10^6$ or $N=10^6$ and $\rho=0.4$. They studied the velocity distributions up to collision time $\tau\simeq300$ for the case with $N=0.5\times10^6$. The simulations reported here go up to $\tau=1000$ for the 2D case, and $\tau=500$ for the 3D case.)

The system is initialized by randomly placing particles in a box. All these particles have the same speed but the velocity vector points in random directions so that $\Sigma_i\vec{v}_i=0$. This system is relaxed to an MB velocity distribution by allowing it to evolve until $\tau\sim100$ with $e=1$, i.e., the elastic limit. This serves as the initial condition for our simulation of inelastic hard spheres.

We will subsequently present results for the time-dependence of the temperature; velocity distribution functions; and the aging of the velocity autocorrelation function. We have obtained results for cases with $e=0.7$, 0.8, 0.9, and 0.95. All statistical results correspond to averages over 50 independent initial conditions.

B. Velocity distributions in the HCS and ICS

1. Two-dimensional case

In Fig. 2, we showed the evolution of the density and velocity fields for the 2D case with $e=0.9$. In Fig. 3, we plot the normalized kinetic energy $E(\tau)/E(0)$ versus τ for the 2D case with $e=0.95$, 0.9, and 0.8. The data is plotted on a linear-log scale—the initial exponential decay corresponds to Haff's cooling law for the HCS. The data deviates from Haff's law when correlations build up in the system. We define the HCS$\rightarrow$ICS crossover time τ_c as the time where the temperature deviates from the Haff prediction by more than 10%. In Table I, we show the values of τ_c in $d=2$ for various values of e.

Next, we examine the velocity distribution functions in the cooling system. In Fig. 4, we plot $v_0P(v,\tau)$ versus v/v_0 (on a linear-log scale) for the 2D case at early times ($\tau\ll\tau_c$), where $P(v,\tau)$ is the speed distribution at time τ. This is obtained as follows. For a particular run, we calculate the quantity

TABLE I. Crossover times from the HCS to the ICS for different values of e in $d=2$. We define the crossover time τ_c as the time when the temperature deviates from the Haff law by more than 10%.

e	τ_c
0.95	82
0.9	32
0.8	13
0.7	8

$$v_0(\tau)=\left[\frac{\sum_{i=1}^{N}\vec{v}_i^{\,2}}{\frac{2}{d}N}\right]^{1/2}. \tag{30}$$

The corresponding speed distribution $P(v,\tau)$ is then computed as a histogram over bins of width $\Delta v=0.08v_0$. To improve statistics, we further average $P(v,\tau)$ over 50 independent runs. In Fig. 4, we show data for $e=0.95$ ($\tau=11$); $e=0.9$ ($\tau=7$); $e=0.8$ ($\tau=4$); and $e=0.7$ ($\tau=1$). The particular choice of τ corresponds to the collision time when our MD data for the second Sonine coefficient (a_2) saturates to the kinetic-theory prediction. (This will be discussed shortly.) The solid line superposed on the data sets corresponds to the MB function in $d=2$:

$$P_{\rm MB}^{d=2}(v)=\frac{2v}{v_0^2}\exp\left(-\frac{v^2}{v_0^2}\right). \tag{31}$$

In a direct plot of the data in Fig. 4, the MD data and the MB function are numerically indistinguishable. In the linear-log plot, the tail of the MD data is seen to systematically differ from the MB function in all cases, though the deviation is

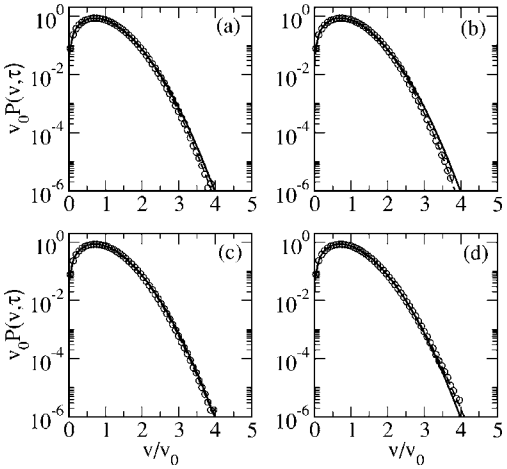

FIG. 4. Scaled velocity distribution, $v_0P(v,\tau)$ vs v/v_0, plotted on a linear-log scale for the $d=2$ case. The data is shown at early times ($\tau\ll\tau_c$) for (a) $e=0.95$ ($\tau=11$); (b) $e=0.9$ ($\tau=7$); (c) $e=0.8$ ($\tau=4$); and (d) $e=0.7$ ($\tau=1$). The solid lines denote the MB distribution in Eq. (31). The dashed lines denote $G(c)$ from Eq. (32), with values of a_2 and a_3 obtained from our MD simulations. These values are provided in Table II.

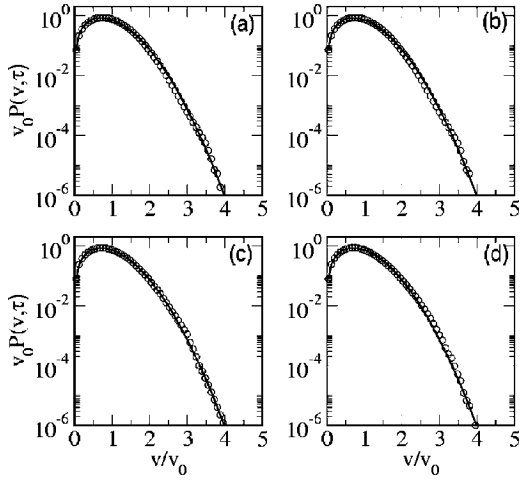

FIG. 5. Analogous to Fig. 4, but at late times ($\tau \gg \tau_c$). All data sets correspond to $\tau=1000$. In this case, we do not plot $G(c)$ from Eq. (32).

small. The dashed line denotes the function ($c=v/v_0$):

$$G(c) = 2ce^{-c^2}[1 + a_2 S_2(c^2) + a_3 S_3(c^2)],$$

$$S_2(c^2) = 1 - 2c^2 + \frac{c^4}{2},$$

$$S_3(c^2) = 1 - 3c^2 + \frac{3c^4}{2} - \frac{c^6}{6}, \tag{32}$$

where the Sonine coefficients a_2, a_3 are calculated from the MD data using Eqs. (20) and (21). The numerical values of these coefficients will be specified shortly. Notice that our MD data does not show *overpopulation of the tail* [$F(\vec{c}) \sim \exp(-Ac)$] [25,30] for the range of c-values over which we have reliable data. This may be attributed to the relatively high values of e in our simulations, and the corresponding high c-values for crossover from the Gaussian tail to the overpopulated tail.

In Fig. 5, we plot $v_0P(v,\tau)$ versus v/v_0 at late times ($\tau \gg \tau_c$), again on a linear-log scale. We show data for $e=0.95$, 0.9, 0.8, and 0.7, all at $\tau=1000$. The solid line denotes the MB function, which is numerically indistinguishable from the MD data on a direct plot. As a matter of fact, even the linear-log plot does not show a systematic discrepancy between the MD data and the MB function. Thus the distribution reverts to a Gaussian at late times. This is due to averaging over a large number of independent clusters, with particle velocities in each cluster being approximately parallel.

For a more quantitative study of the velocity distributions, it is useful to examine the time-dependence of the Sonine coefficients in Eq. (9). The explicit functional forms of a_1 to a_5 were provided in Eqs. (19)–(23). As the initial velocity distribution is of the MB form, $a_n(\tau=0)=0 \forall n>1$. Let us first discuss the behavior of the Sonine coefficient a_2. In Fig. 6, we plot $a_2(\tau)$ versus τ for $d=2$ and $e=0.95$, 0.9, 0.8, and 0.7. We show data for individual runs (dotted lines) and their

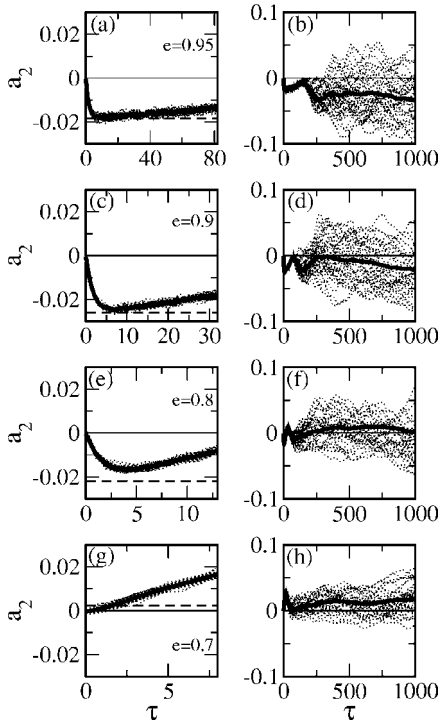

FIG. 6. (a) and (b) Time-dependence of a_2 for $d=2$, $e=0.95$. The dotted lines denote a_2 vs τ for individual runs, and the solid line is the corresponding average. The frames on the left and right show the early time (up to $\tau=\tau_c$) and late-time behaviors, respectively. A horizontal dashed line is drawn in (a) at $a_2 \simeq -0.0186$, corresponding to the NE kinetic-theory prediction in Eq. (17) (Ref. [25]). (c) and (d) a_2 vs τ for $d=2$, $e=0.9$. The dashed line in (c) corresponds to $a_2 \simeq -0.026$. (e) and (f) a_2 vs τ for $d=2$, $e=0.8$. The dashed line in (e) is drawn at $a_2 \simeq -0.0219$. (g) and (h) a_2 vs τ for $d=2$, $e=0.7$. The dashed line in (g) is drawn at $a_2 \simeq 0.0012$.

average (solid line). The frames on the left show the early time behavior (up to $\tau=\tau_c$), and the frames on the right show the behavior for extended times up to $\tau=1000$. In the early HCS ($\tau \ll \tau_c$), the velocity correlations are negligible and the predictions of kinetic theory should apply. For the cases $e=0.95$, 0.9, and 0.8, a_2 saturates to a "steady-state" value on a time scale of $\tau \sim 10$ collisions. The data sets in Figs. 6(a) and 6(c) are consistent with the NE result in Eq. (17)—denoted by a horizontal dashed line in the frames on the left. (Recall that $a_2^{\rm NE}$ and $a_2^{\rm BP}$ are equivalent for this range of e-values, as shown in Fig. 1.) On the other hand, the data sets in Fig. 6(e) (for $e=0.8$) saturate somewhat higher than the value predicted by Eq. (17). Finally, the data sets in Fig. 6(g) (for $e=0.7$) show no sign of settling at the kinetic-theory prediction. Recall that kinetic theory is only applicable when there are no velocity correlations—however, these build up rapidly for $e \ll 1$ and low dimensionality. We define the *saturation time* τ_k as the time when a_2 approaches closest to the kinetic-theory prediction. For the case with $e=0.7$, the data for a_2 versus τ does not show a saturating behavior. In this case, we define τ_k as the time when a_2 crosses the kinetic-theory value—we have $\tau_k=1$ for $e=0.7$. The scaled distributions in Fig. 4 were plotted for $e=0.95$, 0.9, 0.8, and 0.7 at $\tau=\tau_k$.

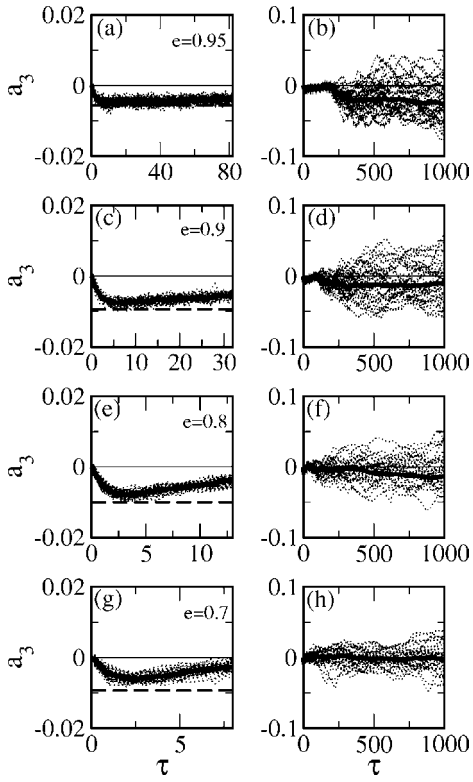

FIG. 7. Analogous to Fig. 6 but for a_3 vs τ. The horizontal dashed lines are drawn at (a) $a_3 \simeq -0.0056$; (c) $a_3 \simeq -0.0094$; (e) $a_3 \simeq -0.0103$; and (g) $a_3 \simeq -0.0093$. These values of a_3 correspond to the BP result in Eq. (25) (Ref. [29]).

In Fig. 6, the frames on the left show that the data sets for individual runs are comparable in the early time regime. However, at later times ($\tau \gg \tau_c$), the individual data sets show strong fluctuations around $a_2 \simeq 0$, in spite of the large system sizes ($N=10^6$) and extensive averaging (50 runs) in our simulations. The ICS consists of clusters of particles streaming in independent directions—an averaging over these clusters is expected to yield a Gaussian distribution of velocities [19,21,37]. Our late-time results are consistent with the MB result $a_2=0$, but the average value of a_2 still shows large variations with τ.

Figure 7 is analogous to Fig. 6, but the data sets correspond to a_3 versus τ. Notice that Fig. 7 has similar features to Fig. 6. However, in this case, even the data for $e=0.7$ approaches the kinetic-theory prediction of BP in Eq. (25). This is denoted by the horizontal dashed lines in Figs. 7(a), 7(c), 7(e), and 7(g).

In Table II, we present average values for a_2, a_3, a_4, and a_5 versus τ for $e=0.95$, 0.9, 0.8, and 0.7. These values are shown for two different times: τ_k, where a_2 first saturates to the kinetic-theory prediction; and τ_c, the HCS→ICS crossover time. We observe that the velocity distributions are primarily described by the coefficients a_2 and a_3—the values of higher coefficients are smaller than a_2 by up to an order of magnitude. In general, the behavior of higher coefficients is analogous to that for a_2 in Fig. 6. There is an early time regime where the data sets for independent runs are approximately coincident. At later times, there is a large variation in the a_n values for various runs—the corresponding averages are consistent with $a_n \simeq 0$.

TABLE II. Numerical values for Sonine coefficients from our $d=2$ MD simulations.

$e=0.95$	$\tau_k=11$	$\tau_c=82$
a_2	−0.0178	−0.0135
a_3	−0.0049	−0.0040
a_4	−0.0006	−0.0010
a_5	−0.00004	−0.0002
$e=0.9$	$\tau_k=7$	$\tau_c=32$
a_2	−0.0246	−0.0177
a_3	−0.0074	−0.0053
a_4	−0.0013	−0.0010
a_5	−0.00001	−0.0001
$e=0.8$	$\tau_k=4$	$\tau_c=13$
a_2	−0.0164	−0.0080
a_3	−0.0076	−0.0039
a_4	−0.0021	−0.0010
a_5	−0.0005	−0.0003
$e=0.7$	$\tau_k=1$	$\tau_c=8$
a_2	0.0010	0.0166
a_3	−0.0048	−0.0026
a_4	−0.0001	−0.0011
a_5	−0.0006	−0.0008

2. Three-dimensional case

In Fig. 8, we show the evolution of the density and velocity fields for the 3D case with $e=0.9$. In Fig. 9, we plot $E(\tau)/E(0)$ versus τ for $e=0.95$, 0.9, and 0.8. Again, the initial decay is described by Haff's law in Eq. (6). As in the 2D case, we define the HCS→ICS crossover time τ_c as the time where the average kinetic energy deviates from the Haff prediction by more than 10%. The corresponding values for $\tau_c(e)$ are shown in Table III.

The scaled velocity distributions for the 3D case show similar behavior as in the 2D case. At early times ($\tau \ll \tau_c$), the tail of the distribution function shows a small but systematic deviation from the MB function. However, at late times ($\tau \gg \tau_c$), the velocity distribution is consistent with the MB

TABLE III. HCS→ICS crossover times for various values of e in $d=3$.

e	τ_c
0.95	251
0.9	97
0.8	37
0.7	22

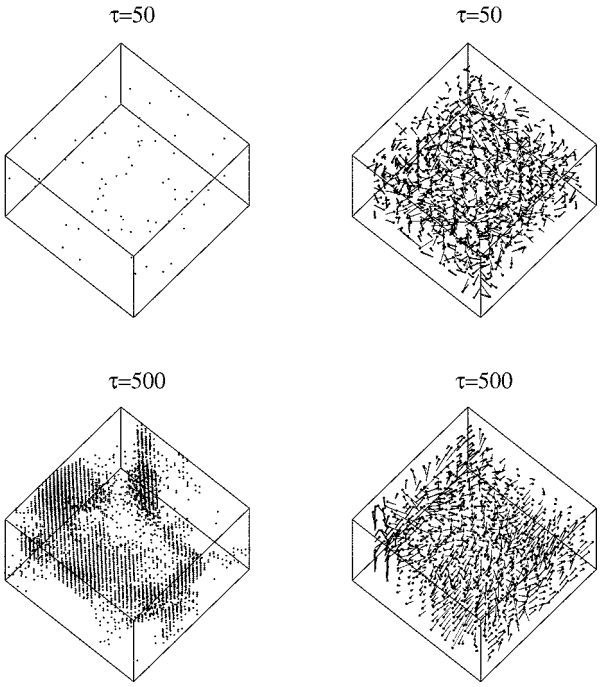

FIG. 8. Analogous to Fig. 2 but for the $d=3$ case. The pictures correspond to $\tau=50$ and 500 for a system with $N=262\,144$, $\phi \simeq 0.105$, and $e=0.9$. The system size is $(109.44\sigma)^3$. The density field (frames on left) is plotted by coarse-graining the system into boxes of size $(3.4\sigma)^3$. Boxes with more than 15 particles are marked black, and other boxes are unmarked. For the velocity field (frames on right), we coarse-grain the system into boxes of size $(10.9\sigma)^3$ and plot the overall velocity vector for each box.

function, though there are fluctuations in the tail region. For the sake of brevity, we do not show the 3D velocity distributions here.

Next, let us study the time-dependence of the Sonine coefficients a_2 and a_3. In Fig. 10, we plot $a_2(\tau)$ versus τ for $d=3$ and $e=0.95$, 0.9, 0.8, and 0.7. Here, we only show results for early times up to $\tau=\tau_c$. As in Fig. 6, the dotted lines denote data from individual runs and the solid line denotes the average value of $a_2(\tau)$ versus τ. The data from individual runs superposes at early times. The coefficient a_2 saturates to the NE prediction in Eq. (17) for $e=0.95$, 0.9—this is denoted by a horizontal dashed line. For $e=0.8$, the "steady-state" value is higher than the kinetic-theory value, as in Fig. 6(e). For $e=0.7$, a_2 does not saturate to its kinetic-theory value at all. The late-time behavior is not shown in this case. As in the 2D case, the data from individual runs shows large variations. The average value of a_2 is consistent with $a_2 \simeq 0$, but is characterized by large fluctuations in spite of the large system sizes and extensive averaging in our MD simulations.

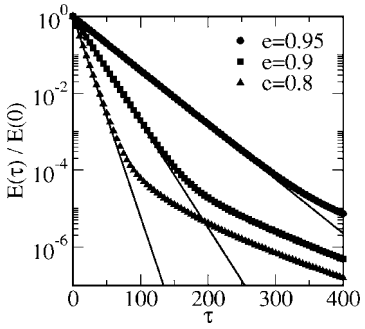

FIG. 9. Analogous to Fig. 3, but for the $d=3$ case.

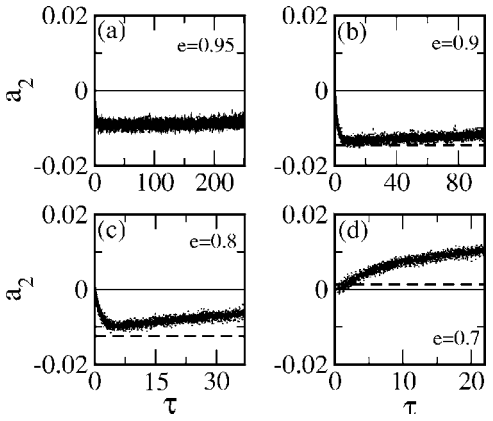

FIG. 10. (a) Time-dependence of a_2 for $d=3$, $e=0.95$. The dotted lines denote a_2 vs τ for individual runs, and the solid line is the average. The frame shows the early time behavior (up to $\tau=\tau_c$). The horizontal dashed line is drawn at $a_2 \simeq -0.0097$, corresponding to the NE result in Eq. (17) (Ref. [25]). (b) a_2 vs τ for $d=3$, $e=0.9$. The dashed line corresponds to $a_2 \simeq -0.0145$. (c) a_2 vs τ for $d=3$, $e=0.8$. The dashed line is drawn at $a_2 \simeq -0.0125$. (d) a_2 vs τ for $d=3$, $e=0.7$. The dashed line is drawn at $a_2 \simeq 0.0018$.

Figure 11 is analogous to Fig. 10, but shows the time-dependence of a_3 for $\tau < \tau_c$. As in the 2D case, the typical values of a_4 and a_5 are up to an order of magnitude smaller than a_2. In Table IV, we present average values of $a_2 \rightarrow a_5$ at two different times (τ_k, τ_c) for $e=0.95$, 0.9, 0.8, and 0.7.

C. Aging of the autocorrelation function

The cooling granular gas is a nonequilibrium system, and the corresponding velocity autocorrelation function exhibits

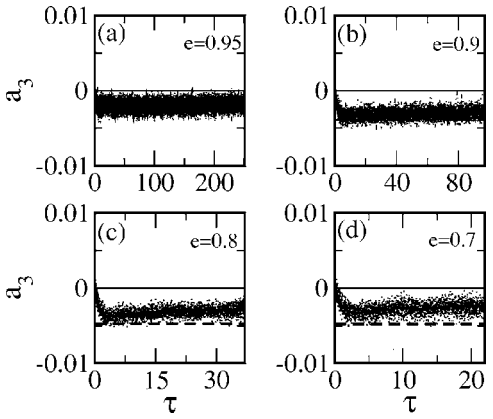

FIG. 11. Analogous to Fig. 10 but for a_3 vs τ. The horizontal dashed lines are drawn at (a) $a_3 \simeq -0.0020$; (b) $a_3 \simeq -0.0039$; (c) $a_3 \simeq -0.0047$; and (d) $a_3 \simeq -0.0048$. These values of a_3 correspond to the BP result in Eq. (28) (Ref. [28]).

TABLE IV. Numerical values for Sonine coefficients from our $d=3$ MD simulations.

$e=0.95$	$\tau_k=8$	$\tau_c=251$
a_2	−0.0091	−0.0080
a_3	−0.0019	−0.0017
a_4	−0.0004	−0.0003
a_5	−0.00001	−0.00004
$e=0.9$	$\tau_k=6$	$\tau_c=97$
a_2	−0.0133	−0.0116
a_3	−0.0033	−0.0028
a_4	−0.0007	−0.0006
a_5	−0.0001	−0.0001
$e=0.8$	$\tau_k=2$	$\tau_c=37$
a_2	−0.0078	−0.0061
a_3	−0.0034	−0.0028
a_4	−0.0011	−0.0008
a_5	−0.0004	−0.0002
$e=0.7$	$\tau_k=1$	$\tau_c=22$
a_2	0.0018	0.0104
a_3	−0.0031	−0.0024
a_4	−0.0009	0.0005
a_5	−0.0005	−0.0004

aging properties [38]. The autocorrelation function is defined as follows:

$$A(\tau_w,\tau)=\frac{1}{N}\sum_{i=1}^{N}\langle\vec{v}_i(\tau_w)\cdot\vec{v}_i(\tau)\rangle, \tag{33}$$

where τ_w is the *waiting time* or the *reference time*. The autocorrelation is computed at τ with respect to the state at τ_w. [The angular brackets in Eq. (33) denote an averaging over independent initial conditions.] For an equilibrium system, $A(\tau_w,\tau)$ depends only on the time difference. However, for nonequilibrium systems, $A(\tau_w,\tau)$ has an explicit dependence on both τ_w and τ. It is straightforward to obtain this dependence in the HCS [39]. Consider the collisions of the particle labeled i. In a small time interval $\Delta\tau$, the velocity of this particle changes from $\vec{v}_i(\tau)$ to $\vec{v}_i(\tau+\Delta\tau)$, where

$$\vec{v}_i(\tau+\Delta\tau)=\begin{cases}\vec{v}_i(\tau) \text{ with probability } 1-\Delta\tau,\\ \vec{v}_i(\tau)-\dfrac{1+e}{2}\{\hat{n}\cdot[\vec{v}_i(\tau)-\vec{u}]\}\hat{n} \text{ with probability } \Delta\tau.\end{cases} \tag{34}$$

In Eq. (34), $\vec{u}$ is chosen from the distribution $P(\vec{u},\tau)$, and the collision direction $\hat{n}$ is drawn from a uniform distribution $\tilde{P}(\hat{n})$. Therefore

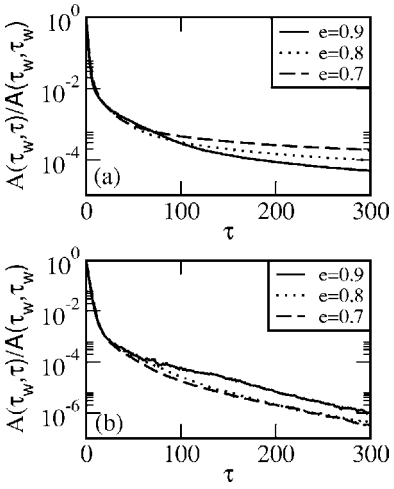

FIG. 12. Autocorrelation functions for the case $\tau_w=0$. We plot $\bar{A}(\tau_w,\tau)=A(\tau_w,\tau)/A(\tau_w,\tau_w)$ vs τ for $e=0.9$, 0.8, and 0.7 and (a) $d=2$, (b) $d=3$.

$$\frac{d}{d\tau}A(\tau_w,\tau)=\lim_{\Delta\tau\to 0}\frac{1}{N}\sum_{i=1}^{N}\overline{\vec{v}_i(\tau_w)\frac{[\vec{v}_i(\tau+\Delta\tau)-\vec{v}_i(\tau)]}{\Delta\tau}}, \tag{35}$$

where the bar denotes an integral over $P(\vec{u},\tau)$ and $\tilde{P}(\hat{n})$. Thus

$$\begin{aligned}\frac{d}{d\tau}A(\tau_w,\tau)&=-\frac{(1+e)}{2}\frac{1}{N}\sum_{i=1}^{N}\int d\vec{u}P(\vec{u},\tau)\int d\hat{n}[\hat{n}\cdot\vec{v}_i(\tau_w)]\\&\quad\times\{\hat{n}\cdot[\vec{v}_i(\tau)-\vec{u}]\}\\&=-\frac{(1+e)}{2d}\frac{1}{N}\sum_{i=1}^{N}\int d\vec{u}P(\vec{u},\tau)[\vec{v}_i(\tau_w)\cdot\vec{v}_i(\tau)\\&\quad-\vec{v}_i(\tau_w)\cdot\vec{u}]\\&=-\frac{(1+e)}{2d}A(\tau_w,\tau).\end{aligned} \tag{36}$$

Thus the autocorrelation function in the HCS decays as

$$\begin{aligned}A(\tau_w,\tau)&=A(\tau_w,\tau_w)\exp\left[-\frac{(1+e)}{2d}(\tau-\tau_w)\right]\\&=dT_0\exp\left(-\frac{\epsilon}{d}\tau_w\right)\\&\quad\times\exp\left[-\frac{(1+e)}{2d}(\tau-\tau_w)\right].\end{aligned} \tag{37}$$

Equation (37) is the appropriate aging form for $A(\tau_w,\tau)$.

Let us first consider the decorrelation of the initial condition. In Fig. 12, we plot the normalized function $\bar{A}(\tau_w,\tau)=A(\tau_w,\tau)/A(\tau_w,\tau_w)$ versus τ for $\tau_w=0$ and $e=0.9$, 0.8, and 0.7. The 2D and 3D cases are shown in Figs. 12(a) and 12(b), respectively. We have confirmed that the early time behavior for $\tau_w=0$ is consistent with Eq. (37). At later times, the decay becomes slower than exponential as velocity correlations build up prior to the ICS.

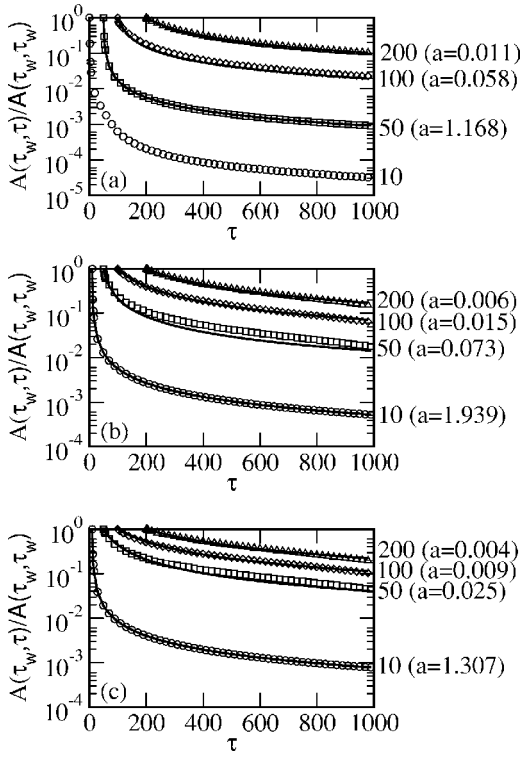

FIG. 13. Autocorrelation functions for the $d=2$ case with different values of the waiting time $\tau_w=10$, 50, 100, and 200. We plot $\bar{A}(\tau_w,\tau)$ vs τ for (a) $e=0.9$; (b) $e=0.8$; and (c) $e=0.7$. The solid lines superposed on the data sets are the best fits to the function $f(\tau)=[1+a(\tau_w)(\tau-\tau_w)]^{-1}$. The best-fit value of $a(\tau_w)$ is specified in the figure.

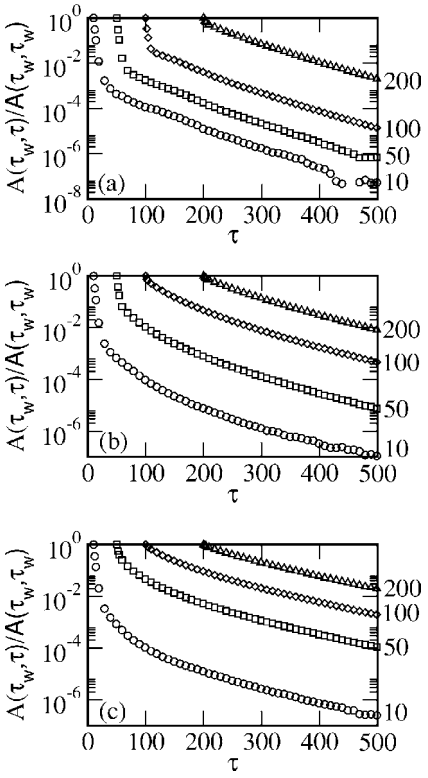

FIG. 14. Autocorrelation functions for the $d=3$ case with different values of the waiting time $\tau_w=10$, 50, 100, and 200. We plot $\bar{A}(\tau_w,\tau)$ vs τ for (a) $e=0.9$; (b) $e=0.8$; and (c) $e=0.7$.

Next, we study the decay of the autocorrelation function for $\tau_w>0$. In Fig. 13, we plot $\bar{A}(\tau_w,\tau)$ versus τ for the 2D case with $e=0.9$, 0.8, and 0.7 and $\tau_w=10$, 50, 100, and 200. Notice that the decay of $\bar{A}$ becomes slower for larger values of the waiting time—this is referred to as the aging property. Further, the decay is slower than the exponential function seen in the HCS. The data sets in Fig. 13 are fitted well by the empirical function:

$$f(\tau)=[1+a(\tau-\tau_w)]^{-1}, \tag{38}$$

where a is a fitting parameter which depends on τ_w. The corresponding fits are shown as solid lines in the figure. At later times, $f(\tau)\sim\tau^{-1}$, which is reminiscent of the long-time tails $A(\tau)\sim\tau^{-d/2}$ of the autocorrelation function for an elastic hard sphere gas [34].

In Fig. 14, we plot $\bar{A}(\tau_w,\tau)$ versus τ for the 3D case with $e=0.9$, 0.8, and 0.7 and $\tau_w=10$, 50, 100, and 200. As in the 2D case, the data sets are characterized by aging, with slower decay for larger values of τ_w. In this case, we were unable to fit the data sets to a simple functional form, perhaps due to the limited time scales available in our simulations. For example, we have examined log-log plots of the data in Fig. 14 and do not see any evidence of an extended power-law regime. We are presently simulating the granular gas (with $N=10^6$) up to $\tau=1000$ for the 3D case also. This is numerically very challenging, but should clarify the functional form of the autocorrelation function in $d=3$.

IV. SUMMARY AND DISCUSSION

Let us conclude this paper with a summary and discussion of the results presented here. We have undertaken large-scale molecular dynamics (MD) simulations of freely evolving granular gases with coefficient of restitution $e\in[0.7,1]$. The system initially loses energy (or cools) in a *homogeneous cooling state* (HCS). At later times ($\tau>\tau_c$, where τ_c is the crossover time), the growth of fluctuations in the density and velocity fields drives the system into an *inhomogeneous cooling state* (ICS). In earlier work [20], we have studied the pattern dynamics in the HCS and ICS, focusing on the evolution morphologies and the cluster growth laws.

Our primary interest in this paper is the nature of velocity distributions [denoted as $P(v,\tau)$] in the HCS and ICS. On a direct plot, it is difficult to distinguish between the MD data for $P(v,\tau)$ and the Maxwell-Boltzmann (MB) distribution function—the differences lie mainly in the tail region. Therefore we model the velocity distributions by a Sonine polynomial expansion [cf. Eq. (9)]. The magnitude of the Sonine coefficients a_n measures the departure from the MB distribution function. For the e-values considered here, the only relevant coefficients are a_2,a_3. The higher coefficients a_4,a_5 are up to an order of magnitude smaller than a_2. Further, for $e=0.95$, 0.9 there is an early time regime where our MD results for a_2 and a_3 are in good agreement with results from

kinetic theory [25,28,29]. This regime becomes more extended for higher dimensionality and as $e \to 1$. At late times ($\tau > \tau_c$), the data sets for a_n versus τ from individual runs show large fluctuations, in spite of the large system sizes ($N=10^6$) used in our simulations. The average values of a_n also show large fluctuations in spite of extensive averaging over 50 runs. The late-time data for a_n is consistent with the MB values ($a_n=0$), but even larger simulations are needed to confirm this conclusively.

In this paper, we have also studied the aging behavior of the velocity autocorrelation function $A(\tau_w, \tau)$, where τ_w is the *waiting time* or *reference time*. In the cooling process, $A(\tau_w, \tau)$ depends on both τ_w and τ. This should be contrasted with the case of a stationary process, where $A(\tau_w, \tau)$ only depends upon the time difference $(\tau - \tau_w)$. When both τ_w and τ lie in the HCS, $A(\tau_w, \tau)$ decays exponentially with τ [cf. Eq. (37)]. We have confirmed that our early time data for $A(\tau_w, \tau)$ obeys Eq. (37). For later times, we observe that the decay of $A(\tau_w, \tau)$ is slower than exponential, and the decay time scale is slower for higher τ_w, i.e., the system exhibits aging. For the $d=2$ case, the data is consistent with the functional form $f(\tau)=[1+a(\tau_w)(\tau-\tau_w)]^{-1}$ over a large range of values of inelasticity e and waiting time τ_w. However, for the $d=3$ case, we are unable to find an approximate functional form for $A(\tau_w, \tau)$.

There remain many open problems in the context of the freely evolving granular gas. In particular, our understanding of the asymptotic ICS remains incomplete. We hope that the results presented here will motivate further analytical and numerical studies of this problem.

ACKNOWLEDGMENTS

The authors are grateful to N. Brilliantov for useful inputs on these problems. In particular, we thank him for sending us his unpublished results on the kinetic theory of the two-dimensional granular gas. S.P. thanks S. Luding, I. Goldhirsch, H. Herrmann, H. Nakanishi, and M. Ernst for useful discussions on the problems discussed here. He is also grateful to the Department of Science and Technology, India for supporting this research through the project *Pattern Formation in Granular Materials*. S.R.A. wishes to thank CSIR, India for financial support.

[1] H. M. Jaeger, S. R. Nagel, and R. P. Behringer, Rev. Mod. Phys. **68**, 1259 (1996).
[2] *Powders and Grains 97: Proceedings of the Third International Conference on Powders and Grains*, edited by R. P. Behringer and J. Jenkins (Balkema, Rotterdam, 1997).
[3] *Powders and Grains 2001: Proceedings of the Fourth International Conference on Powders and Grains*, edited by T. Kishino (Swets and Zeitlinger, Lisse, 2001).
[4] *Powders and Grains 2005: Proceedings of the Fifth International Conference on Powders and Grains*, edited by R. Garcia-Rojo, H. J. Herrmann, and S. Mcnamara (Balkema, Rotterdam, 2005).
[5] G. H. Ristow, *Pattern Formation in Granular Materials* (Springer-Verlag, Berlin, 2000).
[6] J. Duran, *Sands, Powders and Grains* (Springer-Verlag, Berlin, 2000).
[7] N. V. Brilliantov and T. Poschel, *Kinetic Theory of Granular Gases* (Oxford University Press, Oxford, 2004).
[8] F. Melo, P. B. Umbanhowar, and H. L. Swinney, Phys. Rev. Lett. **75**, 3838 (1995); P. B. Umbanhowar, F. Melo, and H. L. Swinney, Nature (London) **382**, 793 (1996).
[9] G. Peng and H. J. Herrmann, Phys. Rev. E **49**, R1796 (1994); **51**, 1745 (1995); O. Moriyama, N. Kuroiwa, M. Matsushita, and H. Hayakawa, Phys. Rev. Lett. **80**, 2833 (1998).
[10] J. Rajchenbach, Phys. Rev. Lett. **65**, 2221 (1990); S. Das Gupta, D. V. Khakhar, and S. K. Bhatia, Chem. Eng. Sci. **46**, 1531 (1991); Powder Technol. **67**, 145 (1991).
[11] O. Zik, D. Levine, S. G. Lipson, S. Shtrikman, and J. Stavans, Phys. Rev. Lett. **73**, 644 (1994).
[12] S. Puri and H. Hayakawa, Physica A **270**, 115 (1999); **290**, 218 (2001).
[13] P. K. Haff, J. Fluid Mech. **134**, 401 (1983).
[14] I. Goldhirsch and G. Zanetti, Phys. Rev. Lett. **70**, 1619 (1993); I. Goldhirsch, M. L. Tan, and G. Zanetti, J. Sci. Comput. **8**, 1 (1993).
[15] S. McNamara and W. R. Young, Phys. Fluids A **4**, 496 (1992); Phys. Rev. E **53**, 5089 (1996).
[16] J. J. Brey, F. Moreno, and J. W. Dufty, Phys. Rev. E **54**, 445 (1996); J. J. Brey, F. Moreno, and M. J. Ruiz-Montero, Phys. Fluids **10**, 2965 (1998); **10**, 2976 (1998).
[17] T. P. C. van Noije, M. H. Ernst, R. Brito, and J. A. G. Orza, Phys. Rev. Lett. **79**, 411 (1997); T. P. C. van Noije, M. H. Ernst, and R. Brito, Phys. Rev. E **57**, R4891 (1998).
[18] S. Luding, M. Huthmann, S. McNamara, and A. Zippelius, Phys. Rev. E **58**, 3416 (1998); S. Luding and S. McNamara, Granular Matter **1**, 113 (1998); S. Luding and H. J. Herrmann, Chaos **9**, 673 (1999).
[19] A. Baldassarri, U. M. Marconi, and A. Puglisi, Phys. Rev. E **65**, 051301 (2002); U. M. B. Marconi, A. Puglisi, and A. Baldassarri, Phase Transitions **77**, 863 (2004).
[20] S. K. Das and S. Puri, Europhys. Lett. **61**, 749 (2003); S. K. Das and S. Puri, Phys. Rev. E **68**, 011302 (2003).
[21] H. Nakanishi, Phys. Rev. E **67**, 010301(R) (2003).
[22] S. R. Ahmad and S. Puri, Europhys. Lett. **75**, 56 (2006).
[23] S. Chapman and T. G. Cowling, *The Mathematical Theory of Non-Uniform Gases* (Cambridge University Press, New York, 1970).
[24] A. Goldstein and M. Shapiro, J. Fluid Mech. **282**, 75 (1995).
[25] T. P. C. van Noije and M. H. Ernst, Granular Matter **1**, 57 (1998).
[26] J. J. Brey, M. J. Ruiz-Montero, and D. Cubero, Phys. Rev. E **54**, 3664 (1996).
[27] M. Huthmann, J. A. G. Orza, and R. Brito, Granular Matter **2**, 189 (2000).
[28] N. V. Brilliantov and T. Poschel, Europhys. Lett. **74**, 424 (2006).

[29] N. V. Brilliantov and T. Poschel (private communication).
[30] S. E. Esipov and T. Poschel, J. Stat. Phys. **86**, 1385 (1997).
[31] R. Brito and M. H. Ernst, Int. J. Mod. Phys. C **8**, 1339 (1998).
[32] T. P. C. van Noije and M. H. Ernst, Phys. Rev. E **61**, 1765 (2000).
[33] J. Wakou, R. Brito, and M. H. Ernst, J. Stat. Phys. **107**, 3 (2002).
[34] M. P. Allen and D. J. Tildesley, *Computer Simulation of Liquids* (Oxford University Press, Oxford, 1987).
[35] D. C. Rapaport, *The Art of Molecular Dynamics Simulation*, 2nd ed. (Cambridge University Press, Cambridge, 2005).
[36] R. Kawahara and H. Nakanishi, J. Phys. Soc. Jpn. **73**, 68 (2004).
[37] X. Nie, E. Ben-Naim, and S. Chen, Phys. Rev. Lett. **89**, 204301 (2002).
[38] J.-P. Bouchaud, L. F. Cugliandolo, J. Kurchan, and M. Mezard, in *Spin Glasses and Random Fields*, edited by A. P. Young (World Scientific, Singapore, 1997), p. 161.
[39] E. Ben-Naim and P. L. Krapivsky, Phys. Rev. E **66**, 011309 (2002).